Combining Simulated and Experimental Data to Simulate Ultrasonic Array Data From Defects in Materials With High Structural Noise

Harry A. Bloxham, Alexander Velichko, and Paul David Wilcox

***Abstract*— Ultrasonic nondestructive testing inspections using phased arrays are performed on a wide range of components and materials. All real inspections suffer, to varying extents, from coherent noise, including image artifacts and speckle caused by complex geometries and grain scatter, respectively. By its nature, this noise is not reduced by averaging; however, it degrades the signal-to-noise ratio of defects and ultimately limits their detectability. When evaluating the effectiveness of an inspection, a large pool of data from samples containing a range of different defects are important to estimate the probability of detection of defects and to help characterize them. For a given inspection, coherent noise is easy to measure experimentally but hard to model realistically. Conversely, the ultrasonic response of defects can be simulated relatively easily. This paper proposes a novel method of simulating realistic array data by combining noise-free simulations of defect responses with coherent noise taken from experimental data. This removes the need for costly physical samples with known defects to be made and allows for large data sets to be created easily.**

***Index Terms*— Array signal processing, copper, image fusion, modelling, noise measurement, phased arrays, ultrasonic imaging, ultrasonic transducer arrays.**

I. Introduction

THE availability of ultrasonic data with accurate signal-to-noise ratios for known defects in industrial inspections is vital to characterize the effectiveness of the inspection. Physical specimens in which an artificial defect has been introduced can be made but such samples are expensive, limiting the pool size. Furthermore, determining the true defect size requires independent nondestructive or destructive measurements, which can be both challenging and expensive. The ability to simulate this data would allow results to be collected for any position and size of defect only at a computational cost. A large data pool created using this method would allow a statistical analysis to be performed and probabilities of detection and false call ratios for given defects to be calculated [1].

All inspections suffer from coherent noise to varying extents. Coherent noise is caused by both the macrogeometry and the microgeometry of the sample. In the context of ultrasonic array imaging, there are two main contributors to this structural coherent noise: image artifacts and speckle. Image artifacts can have many causes, such as mode conversions at interfaces and resonances and reflections in the array transducer itself. These cause additional signals to be received by the array, which are represented by the areas of higher intensity in the final image at locations where no physical feature is present in the specimen. These artifacts are a result of the geometry of the sample and array transducer and will, therefore, appear the same in all samples of the same geometry imaged with the same array.

Metals are formed of a crystalline structure made up of many anisotropic grains with random orientations. Speckle is caused by scattering at these grain boundaries [2]–[4] and becomes significant when the grain size is of the order of the wavelength being used or larger [5]. The observed speckle in the image is a result of the superposition of the array responses from many of these grains with spatial variations dependent on the frequency of the ultrasonic waves. This speckle will vary with the array position but providing the same materials and manufacturing processes are used, the statistical distributions of this speckle in the image will be the same [6] for all samples. For a fixed array position, as with image artifacts, speckle cannot be reduced by averaging.

Modeling the image artifacts accurately requires a 3-D model that accurately captures all relevant physical processes. This is computationally challenging and practically difficult due to the number of adjustable parameters. After multiple reflections, any small error in geometry can lead to a large error in the path taken by the sound wave. In addition, any incident waves will cause mode conversions between longitudinal and shear waves creating many more ray paths, which need to be accounted for adding further complexity to the simulation. Previous work has been done on the modeling of grain scatter using both statistical [7]–[9] and finite element techniques [10], [11], but this too requires complex models. Measuring the coherent noise experimentally from defect-free samples can be done with ease and such samples are relatively cheap and usually abundant in an industrial setting. If such experimental data can be exploited directly in simulations, it would remove the need for complex models of coherent noise and their inherent uncertainties. In contrast to coherent noise simulations, the response of the defect in a noise-free sample of the same geometry can be simulated accurately and at a low computational cost using well-established methods [12].

This paper describes a technique based on superposition that enables a simulated defect response to be accurately merged

Manuscript received September 13, 2016; accepted September 23, 2016. Date of publication September 29, 2016; date of current version December 1, 2016. This work was supported by the U.K. Engineering and Physical Sciences Research Council Industrial CASE Award by BAE Systems Marine Ltd., under Grant 14220026.

The authors are with the Department of Mechanical Engineering, University of Bristol, Bristol, BS8 1TR, U.K. (e-mail: h.bloxham@bristol.ac.uk).

Digital Object Identifier 10.1109/TUFFC.2016.2614492

with experimentally measured noise. This is applied to full matrix capture (FMC) data sets of phased arrays from which any linear array imaging process can be synthesized. Here, the total focusing method (TFM) [13], postprocessing technique, is used. This method artificially focuses the array aperture at every point in the imaging plane, in both transmission and reception, to produce an image of the interior of the component under inspection.

II. Method

A. Ray-Based Modeling

The technique proposed by this paper is valid for combining the response from an experimentally measured defect-free sample with the simulated noise-free response from a defect. The proposed technique is independent of the method used to simulate the defect response. In this paper, a 2-D ray-tracing model is used for the simulation of noise-free ultrasonic data. This 2-D model assumes array elements that are infinitely long in the direction perpendicular to the modeling plane. In reality, array elements have finite length and these cause near-field effects [14], relative to the element length, that are not accounted for in this model.

Although ray-based models are widely used [13], [15], certain aspects require special consideration in the current application, hence a detailed description is provided. This method considers the propagation of ultrasound along ray paths connecting the transmitting and receiving elements of the array. The response for a given transmit–receive pair of elements is the summation of the responses over all possible ray paths connecting the two elements. Although there are an infinite number of such ray paths, it is only necessary to consider the paths that lead to signal arrivals within the time frame of interest.

To determine the path each ray takes, it is first necessary to determine if each feature of the specimen, which has the ability to redirect a wave is spatially large or small relative to the ultrasonic wavelength. Large uniform features, referred to as reflectors, such as the back wall of a sample, appear infinitely large to the incoming wave packet and the angles of incidence and reflection must satisfy Snell's law. At smaller features, referred to as scatterers, diffraction becomes significant and rays must be considered to scatter at any angle. For the purposes of determining the ray paths, each element of the array is considered a point source or receiver and with sensitivity in all the directions. Materials are assumed to be homogeneous on a macroscale and, therefore, each ray path is constructed solely of straight lines. In reality, many materials, which exhibit high structural noise, show some inhomogeneity at a microscale, this causes phase aberrations for any propagating wave front. However, when averaged over many grains, the results were found to be consistent with those calculated assuming a homogeneous material (less than 1-dB error in image). The ray paths considered in this paper are shown in Fig. 1. Mode conversions between longitudinal and shear waves are not considered, because these generally arrive later than the longitudinal wave signals used to form the image, although these can be included if desired.

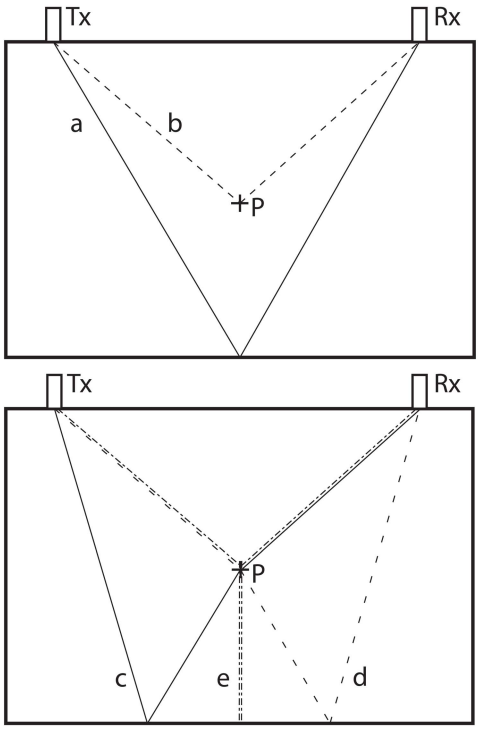

Fig. 1. Direct ray paths, a and b, and secondary ray paths, c, d, and e, in a sample with a scatterer located at P where element Tx is transmitting and element Rx receiving.

The response from the scatterer and the back wall is obtained using rays a and b while rays c, d, and e are used to calculate any shadowing effects the scatterer has on the back wall. Shadowing occurs due to interference between the scattered signals on paths c, d, and e with the directly reflected signal from the back wall on path a. In an image, this results in an area of relatively low intensity along the back wall, typically directly behind the scatterer.

B. Calculating the Ultrasonic Response

The propagation of ultrasound can be modeled in both the time and frequency domains. However, as many interactions are frequency-dependent, calculations are more easily performed in the frequency domain, hence that is the domain used in this model. Once the path of each ray is known, its contribution to the total response can be calculated using the following parameters: the frequency spectrum of the input signal, $F_0(\omega)$; the scattering matrix [16] of the reflector, $S(\phi_t, \phi_r, \omega)$, which is dependent on the angles of the incident and scattered rays, ϕ_t and ϕ_r, respectively; the angular frequency of the signal, ω; and the reflection coefficient of the back wall. For simple defects (e.g., holes and straight cracks), analytical or semianalytical solutions for the scattering matrix exist [12], [17], [18], however, for more complex defects, it must be calculated using numerical methods [19], [20]. For the back wall and other planar reflectors, the amplitude is described by an angle-dependent reflection coefficient, where the angles are defined by Snell's law.

The response from each ray path shown in Fig. 1 must be considered separately, the general technique is given for

ray path a and any modifications required are given for the remaining paths.

1) Ray Path a: The ray-tracing method assumes each element is a point source, and a directivity function, $D(\phi, \omega)$, is used to account for the variation of the ability of each element to transmit and receive at different angles relative to its normal. The exact solution for the directivity of longitudinal and shear waves due to a line source is given by Miller and Pursey [21]. However, for longitudinal waves, $\cos\phi$ provides a reasonable approximation. A sinc term is included as the result of integration over the width of a finite-sized element. The resulting function is

$$D(\phi, \omega) \approx \operatorname{sinc} \frac{\pi a \sin\phi}{\lambda} \cos\phi \tag{1}$$

where a is the element width, ϕ is the angle between the ray and the normal of the element, and λ is the wavelength.

Both the geometric attenuation caused by the beam spreading as the wave propagates and attenuation caused by grain scatter and other losses in the material must also be accounted for. The geometric attenuation A_g^a for a planar interface is calculated using

$$A_g^a = \sqrt{\frac{1}{R_t + R_r}} \tag{2}$$

where R_t and R_r are the distances from the transmission and reception elements to the back wall, respectively. If the array and back wall are parallel, these two distances will be equal. The attenuation due to grain scatter and any other dissipation mechanisms $A_s(\omega)$ is calculated using

$$A_s(\omega) = e^{-\alpha R} \tag{3}$$

where α is the frequency-dependent attenuation coefficient and R is the total propagation distance.

The phase change due to wave propagation $T(\omega)$ is accounted for by the following factor:

$$T(\omega) = e^{-ikR} \tag{4}$$

where k is the wavenumber.

The loss in amplitude due to a reflection (reflection coefficient) from a planar surface (e.g., back wall) for a solid-vacuum interface is given by [22]

$$C_r(\phi_i) = \frac{\cos^2(2\phi_s) - \frac{c_s^2}{c_l^2}\sin(2\phi_s)\sin(2\phi_i)}{\cos^2(2\phi_s) + \frac{c_s^2}{c_l^2}\sin(2\phi_s)\sin(2\phi_i)} \tag{5}$$

where ϕ_i is the angle of incidence at the back wall relative to its normal, ϕ_s is the angle of the reflected shear wave calculated using Snell's law, and c_s and c_l are the shear and longitudinal speeds of sound, respectively.

Using the above parameters, the response, in the frequency domain, due to the input signal propagating along ray path a, can be calculated. There are a number of factors common for all of the ray paths, these are

$$F_{\text{com}}(\omega) = F_0(\omega) D(\phi_t, \omega) D(\phi_r, \omega) A_s(\omega) T(\omega) \tag{6}$$

and the response from ray path a is calculated using

$$F_a(\omega) = F_{\text{com}}(\omega) C_r(\phi_t, \phi_r, \omega) A_g^a. \tag{7}$$

2) Ray Path b: Ray path b is the direct reflection of the defect, and this is calculated in a similar manner to ray path a. However, the scattering matrix for the defect $S(\phi_t, \phi_r, \omega)$, where ϕ_t is the angle of the ray leaving the transmitter and ϕ_r is the angle of the ray received by the reception element, is used instead of the reflection coefficient.

The geometric attenuation is also calculated differently for a scatterer. It is given by

$$A_g^b = \sqrt{\frac{1}{R_t R_r}}. \tag{8}$$

The response due to this ray path is then given by

$$F_b(\omega) = F_{\text{com}}(\omega) S(\phi_t, \phi_r, \omega) A_g^b. \tag{9}$$

3) Ray Paths c and d: Ray paths c and d contain reflections from both a planar interface and a scatterer, therefore, both a reflection coefficient and a scattering matrix are required. The geometric attenuation is defined as in (8) but where R_t is equal to the total ray path length before the scatterer and R_r is the total length after the scatterer.

The response of these ray paths is given by

$$F_c(\omega) = F_{\text{com}}(\omega) C_r(\phi) S(\phi_{\text{rs}}, \phi_r, \omega) A_g^b \tag{10}$$

$$F_d(\omega) = F_{\text{com}}(\omega) C_r(\phi) S(\phi_t, \phi_{\text{ts}}, \omega) A_g^b \tag{11}$$

where ϕ_{rs} is the angle of incident at the scatterer and ϕ_{ts} is the angle of reflection at the scatterer.

4) Ray Path e: Ray path e interacts with the scatterer twice, therefore, two pairs of incident and reflected angles are required. $S_1(\phi_t, \phi_{\text{bw}}, \omega)$ is the first interaction and $S_2(\phi_{\text{bw}}, \phi_r, \omega)$ the second. The angle of incidence at the back wall will always be equal to the back wall normal for this path and defined as ϕ_{bw}, for this case, the reflection coefficient can be approximated as -1, when the back wall is coupled to air. A_g also requires special attention for this path and is defined as follows:

$$A_g^e = \sqrt{\frac{1}{R_t R_s R_r}} \tag{12}$$

where R_t is the ray path length between the transmitter and the scatterer, R_s is the ray path length between the first and second interactions with the scatterer (equal to twice the distance between the scattered and the back wall), and R_r is the path length between the scatterer and receiving element.

The response due to the wave propagating along this path is calculated using

$$F_e(\omega) = -F_{\text{com}}(\omega) S_1(\phi_t, \phi_{\text{bw}}, \omega) S_2(\phi_{\text{bw}}, \phi_r, \omega) A_g^e. \tag{13}$$

The total response for a given transmit–receive pair of elements is then calculated as the sum of the above ray paths

$$F(\omega) = F_a(\omega) + F_b(\omega) + F_c(\omega) + F_d(\omega) + F_e(\omega). \tag{14}$$

This process can then be repeated for all pairs of elements to create an FMC data set. An inverse Fourier transform is then applied to return the data to the time domain

$$f(t) = \frac{1}{2\pi} \int_{-\infty}^{\infty} F(\omega) e^{i\omega t} d\omega \tag{15}$$

where $f(t)$ is the FMC data in the time domain.

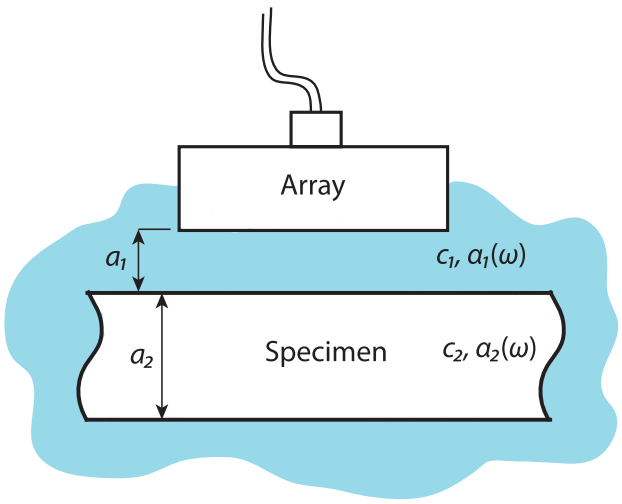

Fig. 2. Schematic of the experimental setup used to calculate F_0 and α. The shaded area represents material 1 (water) and the specimen, material 2.

5) Experimental Measurements: It is assumed that the geometric parameters of the array, test sample, and nominal defect are known accurately. This then allows S, D, A_g, T, and ϕ to be calculated, however, F_0 and α must be determined experimentally. It is possible to measure both of these from a single inspection: an immersion scan of a defect-free plate of known thickness and of the relevant material, as shown in Fig. 2.

Averaging the response of all transmit–receive element pairs is equivalent to using the array as a large unfocused monolithic transducer, whose beam can be assumed to be collimated over the time range of interest. This means that any effects due to beam spreading are negligible. This mean $\bar{u}$ is calculated as follows:

$$\bar{u}(t) = \frac{1}{n^2}\sum_{p=1}^{n}\sum_{q=1}^{n} u_{\mathrm{pq}}(t) \tag{16}$$

where u_{pq} is the signal received, when the pth element is used in transmission and the qth is used in reception and n is the number of elements. By multiplying this by an appropriate Tukey windowing function [23], the front wall and back wall reflections from the test piece can be extracted. The general form of the Tukey function is given by

$$w_t(t) = \begin{cases} 0, & t < t_s \\ \dfrac{1+\cos\left(\frac{2\pi}{r}\left[t - t_s - t_p\frac{r}{2}\right]\right)}{2}, & t_s \le t < t_s + t_p\dfrac{r}{2} \\ 1, & t_s + t_p\dfrac{r}{2} \le t < t_e - t_p\dfrac{r}{2} \\ \dfrac{1+\cos\left(\frac{2\pi}{r}\left[t - t_e + t_p\frac{r}{2}\right]\right)}{2}, & t_e - t_p\dfrac{r}{2} \le t \le t_e \\ 0, & t > t_e \end{cases} \tag{17}$$

where t_s and t_e are the start and end times of the signal of interest, respectively. The windowing function used to extract the front wall signal $w_{fw}(\omega)$ is calculated by setting $t_s = t_1 = (a_1/c_1)$, where a_1 is the depth of water between the array and the test specimen, c_1 is the speed of sound in water, and $t_e = t_1 + t_p$, where t_p is the length of time of the input pulse plus a nominal amount discussed later.

This Tukey window, with parameter r, is equal to unity during the signal of interest and is tapered by a cosine wave at the extremes of this region. The length of each taper is defined as $(r/2)$ multiplied by the length of the region of interest. For this paper, a value of 0.25 was used for r. Due to there being a time delay between time $t = 0$ and the input pulse being emitted, the start of the input signal will occur sometime after t_s. It is important to choose a value of r, such that the true start of the input signal begins after time $t_s + t_p(r/2)$ so that the shape of the input signal is not affected by the windowing function. Because of this delay introduced by the array controller, t_p must be increased by a minimum of an amount equal to this delay plus the length of one taper in the windowing function. This is to ensure that the Tukey window is equal to one over the whole length of the input signal and the tapers are only applied to noise to ensure a zero amplitude start and end to the signal. Similarly, the back wall windowing function, $w_{\mathrm{bw}}(t)$, is calculated by setting $t_s = t_1 + t_2$ and $t_e = t_1 + t_2 + t_p$, where $t_2 = (a_2/c_2)$, and a_2 is the thickness of the specimen and c_2 is the speed of sound in the specimen.

Using a Fourier transform, the relevant windowed signal can be converted into the frequency domain. These are defined as $F_1(\omega)$ for the front wall and $F_2(\omega)$ for the back wall and are calculated using

$$\begin{aligned} F_1(\omega) &= \int_{-\infty}^{\infty} \bar{u}(t) w_{fw}(t) e^{i\omega t}\,dt \\ &= F_0(\omega) e^{-2a_1\alpha_1(\omega)} R_{12} \end{aligned} \tag{18}$$

$$\begin{aligned} F_2(\omega) &= \int_{-\infty}^{\infty} \bar{u}(t) w_{\mathrm{bw}}(t) e^{i\omega t}\,dt \\ &= F_0(\omega) e^{-2a_1\alpha_1(\omega)} T_{12} e^{-2a_2\alpha_2(\omega)} R_{23} T_{21} \end{aligned} \tag{19}$$

where $\alpha_1(\omega)$ is the attenuation coefficient in water and $\alpha_2(\omega)$ is the attenuation coefficient in the specimen. R_{12} and T_{12} are the reflection and transmission coefficients [22] traveling from material 1 to material 2, respectively, where material 1 is on the array side of the sample, material 2 is the sample, and material 3 is on the far side of the sample. For most immersion tests, materials 1 and 3 will be identical, however, for cases, such as *in situ* pipes they may differ.

By comparing the frequency spectra of these two signals, it is possible to calculate the attenuation coefficient $\alpha(\omega)$

$$\alpha(\omega) = -\ln\left|\frac{F_2(\omega)}{F_1(\omega)}\frac{R_{12}}{T_{12}R_{23}T_{21}}\right|\frac{1}{2a_2}. \tag{20}$$

In practice, noise in $F_1(\omega)$ and $F_2(\omega)$ prevents accurate calculations of $\alpha(\omega)$ at the extremes of the bandwidth of the input signal. For this reason, (20) is applied over the -6-dB bandwidth of the transducer and cubic extrapolation is used to obtain attenuation values for the full bandwidth of the transducer.

Once $\alpha(\omega)$ is known, it is then possible to calculate the input signal, $F_0(\omega)$. To remove any effect coupling has on the input signal, it is best to extract the input signal directly from the

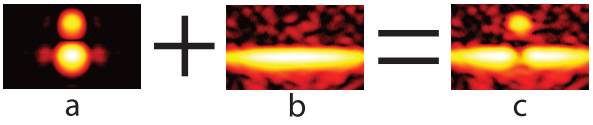

Fig. 3. (c) Superposition of (a) noise-free simulated defect and shadowing effects with (b) experimentally measured back wall.

experimental defect-free data set to which the defect response will be combined, as described in Section II-C. However, this requires the data to contain a strong signal from a flat back wall. If this data set is not suitable, it is possible to extract it from an alternative defect-free inspection of the same type (i.e., contact, immersion, and so on) and material.

Described below is the technique to calculate the input signal from a contact inspection of a sample with a large back wall parallel to the array. First, the mean of the pulse-echo signals $\bar{u}_{\mathrm{pe}}(t)$ is calculated and a windowing function is applied

$$\bar{u}_{\mathrm{pe}}(t) = w_{\mathrm{bw}}(t)\frac{1}{n}\sum_{j=1}^{n} u_{jj}(t) \tag{21}$$

where $w_{\mathrm{bw}}(t)$ is calculated using (17), as it is a contact inspection, $t_0 = 0$, therefore, t_s and t_e are equal to t_1 and $t_1 + t_p$, respectively. This signal is then shifted on the time axis so that the first nonzero value of the windowing function occurs at $t = 0$. The input signal is then calculated by correcting for attenuation using the following equation:

$$F_0(\omega) = \frac{\bar{U}_{\mathrm{pe}}(\omega)}{A_s(\omega)A_g} \tag{22}$$

where $\bar{U}_{\mathrm{pe}}(\omega)$ is the frequency spectrum of $\bar{u}_{\mathrm{pe}}(t)$ and $A_s(\omega)$ and A_g are calculated using (3) and (2), respectively. This procedure of back propagating a measured back wall signal using the inverse of the process used in the forward model guarantees agreement between simulated and measured back wall signals. This agreement is crucial for the success of the technique described by this paper.

C. Combining Simulated and Experimental Data

This paper proposes a novel method of simulating data of defects in high structural noise samples. The superposition of a defect-free experimental data set and a simulated defect including any relevant shadowing effects (ray paths b, c, d, and e) will result in a data set, which is equivalent to the defect being present in the sample. This is shown schematically in Fig. 3.

Assuming there are negligible errors in phase and amplitude between the experimental back wall and simulated defect data, a simple summation of these two sets of signals will provide a superposition that is equivalent to the defect being present in the noisy experimental data. The back wall shadowing effects occur due to the signal produced by the model interfering destructively with the back wall signal. The nature of this interference means that this superposition is very sensitive to any relative error in phase between the simulated signals and the experimental data. The data used in this paper are sampled at 50 MHz, at this frequency, a relative time error of 1 time step between the simulated and experimental data is equal to approximately a 24° phase error. For the defect, an error of this size would result in a position error in the image of approximately 0.1 mm, smaller than one pixel in the images seen in Fig. 5 and can be considered negligible. However, for the back wall, this same error results in an amplitude change of the order of 6 dB, for the defect shown in Fig. 5(a), at the area of the back wall most affected by shadowing. To achieve this negligible error in phase, it is important that the speed of sound and specimen thickness used to calculate $w_{\mathrm{bw}}(t)$ in (21) is known precisely for the conditions in which the experimental results were obtained. This is so that the back wall signal can be back propagated accurately to time $t = 0$ to be used as the input signal. The most significant source of amplitude errors in the simulation is due to errors in $\alpha(\omega)$, the accurate measurement of which is notoriously difficult. However, as the experimental signal is back propagated to get the input signal, then forward propagated using the same $\alpha(\omega)$, the errors associated with $\alpha(\omega)$ will be proportional to the difference in length between the ray path in question and the pulse-echo back wall ray path. This means that the closer to the back wall the defect is, the more accurate the model will be. Defects in close proximity to the back wall generally cause the largest levels of shadowing and due to this will require a more precise model to simulate accurately. This method ensures that the errors are minimized for the defect and shadowing effects that are hardest to reproduce.

III. Results

A. Validation of the Model

To validate this method, a comparison was made between simulated and experimental results for the case of side-drilled holes and back walls in a copper sample. The scattering matrix for the side-drilled hole was calculated using the exact, analytical solution given by [17]. Ultrasonic attenuation in copper has been studied extensively [24] and it was chosen as a suitable material for this research. By varying the array center frequency between 2.5 and 8 MHz, the attenuation and speckle vary from relatively little (14-dB drop in 6-cm-thick sample) to almost complete attenuation (220-dB drop in same sample) in the sample used, this allows for the level of image speckle to be chosen using a single sample by changing the array or filter frequency.

A stepped sample was made with back walls located at depths of 20, 40, 60, and 65 mm and 1.5-mm-diameter side-drilled holes at depths of 5, 20, 40, and 60 mm over back walls 65 mm deep. Using a 64 element, 2.5-MHz array, an immersion test of the 20-mm back wall was used to calculate $\alpha(\omega)$, and $F_0(\omega)$ was calculated from a contact inspection of the 65-mm-deep back wall. This array was then used to image the back walls and defects, and the amplitudes of these were compared with the equivalent simulated results. The amplitude values quoted below were calculated by taking the maximum amplitude of a TFM image at the back wall or defect. The values for the defects are normalized to a 65-mm-deep

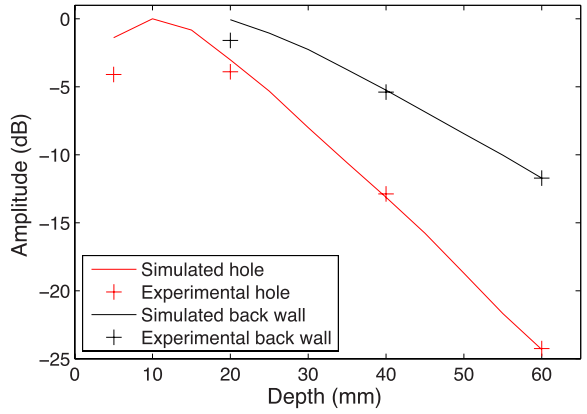

Fig. 4. Amplitude drop for experimental and simulated back walls and holes.

back wall, which is present in all of the images. As there is no constant feature in the back wall images to normalize from, the absolute amplitudes are normalized to the 60-mm-deep back wall. As the model back propagates the input signal from an experimentally measured 65-mm-deep back wall, the specific reflector can be assumed to be correct in the model regardless of any inaccuracies present in the simulation so is, therefore, an ideal reflector to use as a reference to normalize from.

Fig. 4 shows how the predicted image amplitude of a scatterer (side-drilled hole) and planar reflector (back wall) vary with respect to their depths in a simulated test sample. In addition, shown on the figure are experimentally measured scatterer amplitudes (obtained from samples containing actual side-drilled holes at various depths) and planar reflector amplitudes (obtained from the back walls of the samples of different thicknesses). It can be seen that the model, using $\alpha(\omega)$ calculated, as described in Section II-B5, accurately predicts the image amplitudes of both planar reflectors (modeled using only ray path a) and scatterers (modeled using only ray path b) at depths greater than 40 mm. At depths of 20 mm and below, the limitations of this 2-D model can be seen as the experimental results diverge from the simulated amplitudes. These results show that the 2-D model used is sufficiently accurate at propagation distances equivalent to a depth of 40 mm and greater in copper. Therefore, these depths were used for further analysis of the model.

The effectiveness of this technique at simulating realistic images of defects using the method described in Section II-C was also investigated. Fig. 5 shows a comparison between experimental and simulated images of a defect. The simulated image was created by combining an experimental back wall data set with simulated defect data. This was done for two different depths of the defect and a very good visual agreement can be seen between the purely experimental data and the combined data sets both in terms of the amplitude and size of the defect in the image and back wall shadowing effects.

Figs. 6 and 7 show the image amplitudes for horizontal cross sections taken at the center of the defect [Figs. 6(a) and 7(a)] and at the center of the back wall [Figs. 6(b) and 7(b)] for the inspections, as shown in Fig. 5. A single experimental

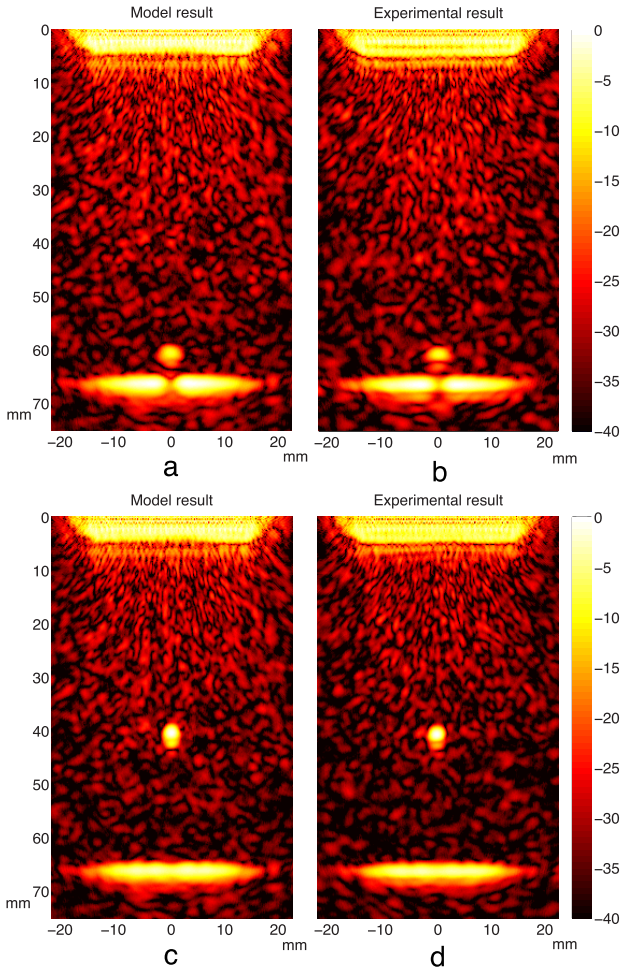

Fig. 5. TFM images for a 1.5-mm (1.06λ) diameter hole located (a) and (b) 5 mm from the back wall and (c) and (d) 25 mm from the back wall. (a) and (c) use combined data sets, while (b) and (d) are the experimental results. The array used has a nominal center frequency of 2.5 MHz and has been filtered at a frequency of 3.25 with a half bandwidth of 1.75 MHz. The imaging plane is 50 mm $\times$ 75 mm.

result is shown and compared with a range of results from the model, each with a different realization of coherent noise. These results quantify the visual similarities seen in Fig. 5 and it can be seen that the defect shape and amplitude are accurately modeled.

Each image is normalized to the point of maximum amplitude in that image. The absolute amplitude of this point is subject to variations due to noise, as this point is always equal to 0 dB in the image, these variations have the effect of changing the amplitude at every other point in the image by an equal amount, on a linear scale. This effect is best seen in Fig. 7(a). This shows a very good agreement for the defect shape between approximately x-positions -2 and 2 mm (outside of this range the response is dominated by noise, so large variations are expected) and identical maximum amplitudes of 0 dB as, for this case, the rest of the image is normalized to the center of this defect. The model results for the back wall amplitudes shown in Fig. 7(b) show significant variation, this is due to the compounded effects of

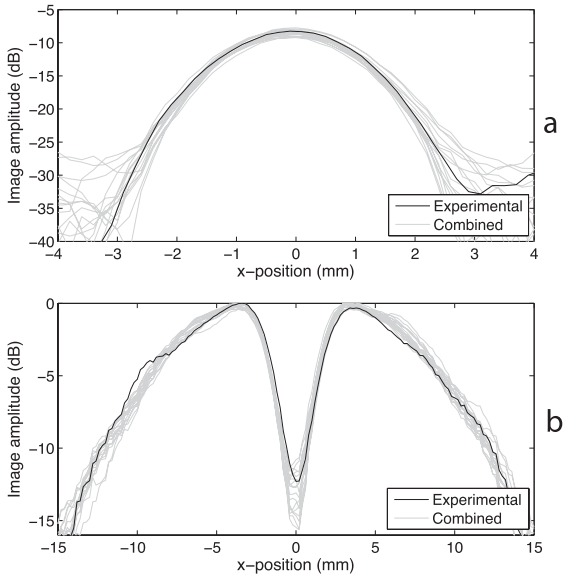

Fig. 6. Image amplitude cross sections of a 1.5-mm (1.06λ) diameter hole located 5 mm from the back wall and 60 mm from the array. (a) At the depth of the hole. (b) At the depth of the back wall. Experimental measurements from a sample containing a physical hole are shown in black and results from multiple defect-free experimental measurements combined with modeled data from a hole are shown in gray.

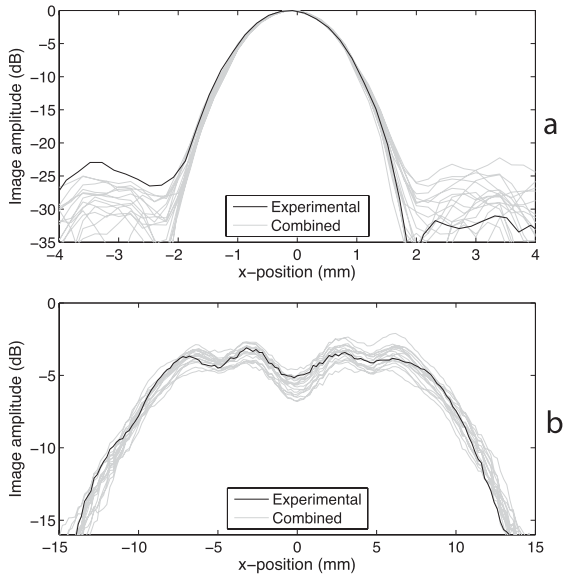

Fig. 7. Image amplitude cross sections of a 1.5-mm (1.06λ) diameter hole located 25 mm from the back wall and 40 mm from the array. (a) At the depth of the hole. (b) At the depth of the back wall. Experimental measurements from a sample containing a physical hole are shown in black and results from multiple defect-free experimental measurements combined with modeled data from a hole are shown in gray.

the noise associated with the point of maximum amplitude (uniform linear shift for whole back wall) and noise local to the back wall (different for each point in the image). The experimental result shown in the same figure has a similar shape and amplitude within the range of those predicted by the model, suggesting that the model provides realistic results.

The images used for the data shown in Fig. 6 are normalized to a point on the back wall. This causes a shift in amplitude at the defect in addition to its localized noise, which is seen in Fig. 6(a). There are large variations seen in the back wall amplitude at the center of the image where the shadowing effects occur. This is likely due to the sensitivity of interference between the back wall and its shadowing effects, on which noise may have an effect more significant than would be expected at any other point in the image.

B. Statistical Studies

The potential of this technique applied to the statistical analysis of an inspection is demonstrated here. The example used is a study to determine which orientations of a fixed size crack at a fixed location are detectable for the given inspection. A similar process can be applied for any study requiring a large pool of defect data.

The ultrasonic response from a 1-mm crack with its center located 5 mm from the back wall in a copper specimen 65 mm deep was simulated with the crack inclined at various angles from horizontal from 0° to 90°. The scattering matrix for the crack was calculated using the semianalytical method, developed in [25], which is based on the boundary integral equation method. These results were then combined with 20 independent defect-free experimental data sets to provide the data on which this statistical study is based. As the crack rotates from horizontal, its amplitude in the image decreases. At a certain angle, the amplitude drops below the level of the image noise and becomes indistinguishable from the speckle, this can be seen to occur between Fig. 8(c) and (d).

A threshold amplitude of the rms noise +12 dB was chosen to determine if any point in the image is a defect. The choice of this threshold is arbitrary and depends on external factors for a particular inspection, which typically involve balancing the costs of false positives (false calls) with detection sensitivity. The effect of the threshold on false call rate can be estimated, if the image grain noise is assumed to have a Rayleigh distribution (the expected amplitude distribution for fully developed speckle) and to have a spatial correlation length of one wavelength (1.4 mm) then a threshold 12 dB above the rms level is expected to result in a 0.46% false call rate per image of the size, as shown in Fig. 5. Fig. 9 shows how this threshold level compares with the image amplitude for the crack at a range of angles. The minimum defect amplitude was calculated at a 97.5% confidence level, using this, it can be seen that this defect falls under the threshold value at a crack angle of greater than 40°.

A maximum detectable crack angle of 40° covers only 44.4% of possible orientations. Assuming real life cracks are randomly oriented, this paper shows that using only the image amplitude to identify the defect will result in the majority of 1-mm cracks not being detected at the 97.5% confidence level. However, by analyzing the back wall amplitude, it can be seen that shadowing effects cause a statistically significant amplitude drop for the full range of crack angles, these results can be seen in Fig. 10. Studies such as these could be used to better understand the detectability of a variety of defects for any given inspection and requires only defect-free experimental results.

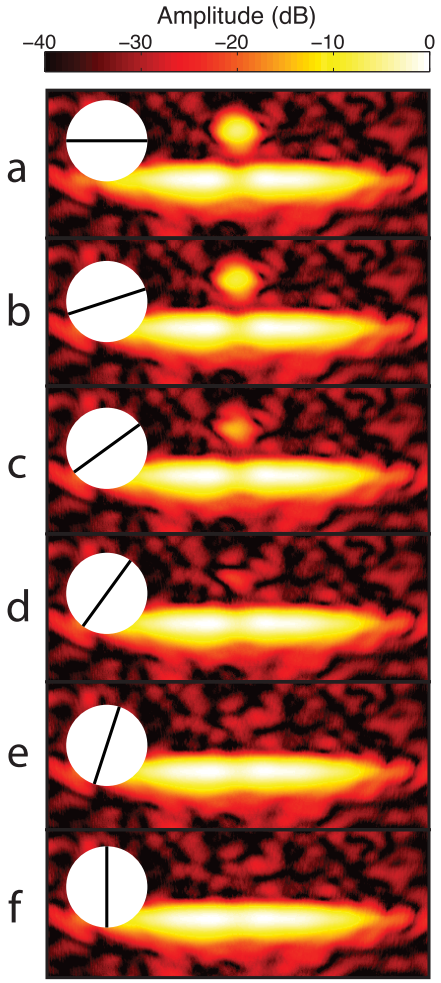

Fig. 8. TFM images for a 1-mm (0.71λ) crack located 5 mm from the back wall of a 65-mm-deep specimen inclined at (a) 0°, (b) 18°, (c) 36°, (d) 54°, (e) 72°, and (f) 90° anticlockwise from horizontal with a crack angle schematic inset. The same array and filter as Fig. 5 has been used.

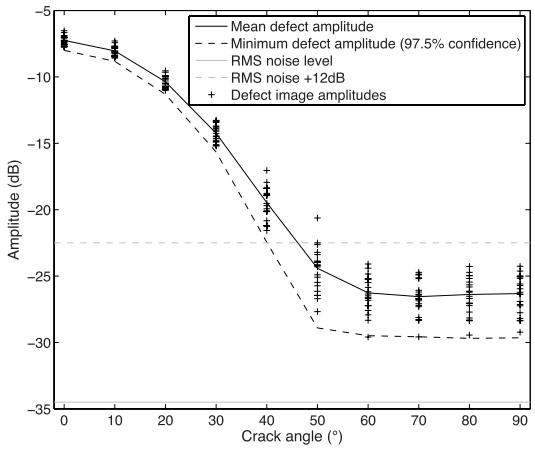

Fig. 9. Defect image amplitude versus crack angle for a 1-mm crack located 5 mm from the back wall of a 65-mm-deep copper sample.

IV. Conclusion

It had been shown that the proposed technique for combining a simulated defect response with experimentally measured structural noise is capable of producing realistic images of an inspection, as seen in Fig. 5. Figs. 6 and 7 show that these images have accurate amplitudes for both defects and back walls, including shadowing effects. Some accuracy is lost at the point of maximum shadowing when the total shadowing effects are large. However, these shadowing effects are primarily useful to study when the defect is on, or past, the limit of detectability. In such cases, the shadowing effects will generally be lower and the model will provide more accurate results. Inspections with large shadowing effects have been included in this paper to show that all of the dominant physical processes are accounted for in the model.

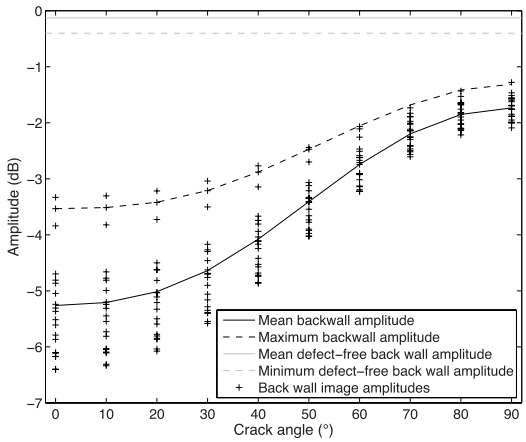

Fig. 10. Back wall image amplitude versus crack angle for a 1-mm crack located 5 mm from the back wall of a 65-mm-deep copper sample. The minimum defect-free back wall amplitude is calculated at a 99.9% confidence level and the maximum back wall amplitude is calculated at the 97.5% confidence level.

This technique has only been validated for a single defect type and only at two depths; however, Fig. 4 shows that the model is capable of accurately predicting amplitudes for both back walls and holes at a range of depths. In addition, as this method calculates the defect response using a scattering matrix, it can be assumed to be valid for any defect if the scattering matrix being used has been independently validated.

Section III-B describes an example of how this technique may be used to find the limits of defect detectability of an inspection. Similar methods could be utilized to study the effectiveness of any inspection, which would traditionally require a large pool of experimentally obtained defect data. Such a pool would be costly to create due to the difficulty of introducing defects to the samples in a controlled manner. The methods discussed in this paper allow for extremely large pools of defect data in noisy samples to be created using only defect-free experimental data, which can be obtained cheaply. In addition, one set of defect-free data can be combined with an unlimited number of simulated defect types and positions rather than a new set of samples and experimental results be collected for each new defect analyzed.

References

[1] J. D. Achenbach, "Quantitative nondestructive evaluation," *Int. J. Solids Struct.*, vol. 37, nos. 1–2, pp. 13–27, Jan. 2000.

[2] A. Li, R. Roberts, F. J. Margetan, and R. R. Thompson, "Study of the effect of microstructure on ultrasonic signal attenuation," *Rev. Prog. Quant. Nondestruct. Eval.*, vol. 557, pp. 1322–1329, Apr. 2001.

[3] H. B. Huntington, "On ultrasonic scattering by polycrystals," *J. Acoust. Soc. Amer.*, vol. 22, no. 3, pp. 362–364, 1950.
[4] E. P. Papadakis, "Ultrasonic attenuation caused by scattering in polycrystalline media," *J. Acoust. Soc. Amer.*, vol. 37, no. 4, pp. 711–717, 1965, doi: http://dx.doi.org/10.1121/1.1909401.
[5] W. P. Mason and H. J. McSkimin, "Energy losses of sound waves in metals due to scattering and diffusion," *J. Appl. Phys.*, vol. 19, no. 10, pp. 940–946, 1948.
[6] R. F. Wagner, S. W. Smith, J. M. Sandrik, and H. Lopez, "Statistics of speckle in ultrasound B-scans," *IEEE Trans. Sonics Ultrason.*, vol. 30, no. 3, pp. 156–163, May 1983.
[7] F. S. Cohen, "Modeling of ultrasound speckle with application in flaw detection in metals," *IEEE Trans. Signal Process.*, vol. 40, no. 3, pp. 624–632, Mar. 1992.
[8] F. J. Margetan, R. B. Thompson, and I. Yalda-Mooshabad, "Modeling ultrasonic microstructural noise in titanium alloys," in *Review of Progress in Quantitative Nondestructive Evaluation*, D. Thompson and D. E. Chimenti, Eds. New York, NY, USA: Springer, 1993, pp. 1735–1742.
[9] I. Yalda, F. J. Margetan, and R. B. Thompson, "Predicting ultrasonic grain noise in polycrystals: A Monte Carlo model," *J. Acoust. Soc. Amer.*, vol. 99, no. 6, pp. 3445–3455, Jun. 1996.
[10] A. Van Pamel, P. Huthwaite, C. R. Brett, and M. J. S. Lowe, "A finite element model investigation of ultrasonic array performance for inspecting polycrystalline materials," in *Proc. 41st Annu. Rev. Prog. Quant. Nondestruct. Eval.*, vol. 34, 2015, pp. 1007–1014.
[11] G. Ghoshal and J. A. Turner, "Numerical model of longitudinal wave scattering in polycrystals," *IEEE Trans. Ultrason., Ferroelect., Freq. Control*, vol. 56, no. 7, pp. 1419–1428, Jul. 2009.
[12] L. W. Schmerr, Jr., *Fundamentals of Ultrasonic Nondestructive Evaluation—A Modeling Approach*. New York, NY, USA: Plenum Press, 1998.
[13] C. Holmes, B. W. Drinkwater, and P. D. Wilcox, "Post-processing of the full matrix of ultrasonic transmit–receive array data for non-destructive evaluation," *NDT&E Int.*, vol. 38, no. 8, pp. 701–711, Dec. 2005.
[14] P. R. Stepanishen, "Transient radiation from pistons in an infinite planar baffle," *J. Acoust. Soc. Amer.*, vol. 49, no. 5B, pp. 1629–1638, 1971.
[15] E. Iakovleva, S. Chatillon, P. Bredif, and S. Mahaut, "Multi-mode TFM imaging with artifacts filtering using CIVA UT forwards models," in *Proc. 40th Annu. Rev. Progr. Quant. Nondestruct. Eval., Incorporating 10th Int. Conf. Barkhausen Noise Micromagn. Test.*, vol. 33. 2014, pp. 72–79.
[16] V. Varatharajulu and Y.-H. Pao, "Scattering matrix for elastic waves. I. Theory," *J. Acoust. Soc. Amer.*, vol. 60, no. 3, pp. 556–566, 1976.
[17] R. M. White, "Elastic wave scattering at a cylindrical discontinuity in a solid," *J. Acoust. Soc. Amer.*, vol. 30, no. 8, pp. 771–785, 1958.
[18] A. L. Lopez-Sanchez, H.-J. Kim, L. W. Schmerr, Jr., and A. Sedov, "Measurement models and scattering models for predicting the ultrasonic pulse-echo response from side-drilled holes," *J. Nondestruct. Eval.*, vol. 24, pp. 83–96, Sep. 2005.
[19] P. D. Wilcox and A. Velichko, "Efficient frequency-domain finite element modeling of two-dimensional elastodynamic scattering," *J. Acoust. Soc. Amer.*, vol. 127, pp. 155–165, Jan. 2010.
[20] J. Zhang, B. W. Drinkwater, and P. D. Wilcox, "Defect characterization using an ultrasonic array to measure the scattering coefficient matrix," *IEEE Trans. Ultrason., Ferroelect., Freq. Control*, vol. 55, no. 10, pp. 2254–2265, Oct. 2008.
[21] G. F. Miller and H. Pursey, "The field and radiation impedance of mechanical radiators on the free surface of a semi-infinite isotropic solid," *Proc. Roy. Soc. London Math. Phys. Eng. Sci.*, vol. 223, no. 1155, pp. 521–541, May 1954.
[22] H. G. Tattersall, "The ultrasonic pulse-echo technique as applied to adhesion testing," *J. Phys. D, Appl. Phys.*, vol. 6, no. 7, pp. 819–832, 1973.
[23] F. J. Harris, "On the use of windows for harmonic analysis with the discrete Fourier transform," *Proc. IEEE*, vol. 66, no. 1, pp. 51–83, Jan. 1978.
[24] X.-G. Zhang, W. A. Simpson, Jr., J. M. Vitek, D. J. Barnard, L. J. Tweed, and J. Foley, "Ultrasonic attenuation due to grain boundary scattering in copper and copper-aluminum," *J. Acoust. Soc. Amer.*, vol. 116, pp. 109–116, Jul. 2004.
[25] E. Glushkov, N. Glushkova, A. Ekhlakov, and E. Shapar, "An analytically based computer model for surface measurements in ultrasonic crack detection," *Wave Motion*, vol. 43, pp. 458–473, Jun. 2006.

Harry A. Bloxham was born in Manchester, U.K., in 1991. He received the M.Eng. degree in mechanical engineering from the University of Bristol, Bristol, U.K., in 2014. He is currently pursuing the Ph.D. degree in engineering with the Ultrasonics and Nondestructive Testing Group, University of Bristol, with a focus on the improving simulations of the ultrasonic images of defects in noisy materials.

Alexander Velichko was born in Krasnodar, Russia, in 1975. He received the M.Sc. degree in applied mathematics from the Kuban State University, Krasnodar, Russia, in 1998, and the Ph.D. degree from the Rostov State University, Rostov-on-Don, Russia, in 2002, with a focus on the investigation of wave fields caused by internal vibration sources in layered elastic medium.

From 2005 to 2012, he was a Research Associate with the Ultrasonics and Nondestructive Testing Research Group, University of Bristol, Bristol, U.K. In 2012, he was appointed Lecturer with the Department of Mechanical Engineering, University of Bristol. His current research interests include the mathematical modeling of propagation and the scattering of elastic waves, ultrasonic imaging using arrays, and guided waves and signal processing.

Paul David Wilcox was born in Nottingham, U.K., in 1971. He received the M.Eng. degree in engineering science from the University of Oxford, Oxford, U.K., in 1994, and the Ph.D. degree from Imperial College London, London, U.K., in 1998.

From 1998 to 2002, he was a Research Associate with the Nondestructive Testing Research Group, Imperial College London, where he was involved in the development of guided wave array transducers for large area inspection. From 2000 to 2002, he was a consultant to Guided Ultrasonics Ltd., Nottingham, U.K., a manufacturer of guided wave test equipment. He held an EPSRC Advanced Research Fellowship in Quantitative Structural Health Monitoring from 2007 to 2012. He has been with the Department of Mechanical Engineering, University of Bristol, Bristol, U.K., since 2002, where he is currently a Professor of Dynamics. His current research interests include array transducers, embedded sensors, ultrasonic particle manipulation, long-range guided wave inspection, structural health monitoring, elastodynamic scattering, and signal processing.